Published in final edited form as:
Magn Reson Med. 2017 February ; 77(2): 623–634. doi:10.1002/mrm.26145.

Single-scan magnetic resonance imaging with exceptional resilience to field heterogeneities

Zhiyong Zhang[a,b], **Amir Saginer**[a], and **Lucio Frydman**[a,*]

[a]Department of Chemical Physics, Weizmann Institute of Science, Rehovot 76100, Israel

[b]Department of Electronic Science, Fujian Provincial Key Laboratory of Plasma and Magnetic Resonance, Xiamen University, Xiamen, Fujian 361005, China

Abstract

An approach delivering single-scan MRI with unprecedented resilience to field inhomogeneities, is proposed and illustrated. The method departs from conventional *k*-based scanning methods, and relies instead on spatiotemporally encoding the image being sought. Unlike hitherto proposed methods, however, this MRI image readout does not take place utilizing a magnetic field gradient along the direction being probed, but rather with the aid of an ancillary source of inhomogeneous frequency broadening. This ancillary dimension can arise from an orthogonal field gradient, from susceptibility- or shift-imposed frequency distributions, from intrinsic spin anisotropies, or from a combination of these all. By allowing such broadenings to act as the agents that spatiotemporally encode and readout the desired imaging information, the ensuing MR images become insensitive to the presence of field inhomogeneities or internal shifts. Even when dealing with notably distorted spin-echo multi-scan images acquired in low-homogeneity magnets or next to metallic objects, the new approach delivers unbiased single-shot images. The principles and characteristics of this new approach – compatible with existing scanners and free from the need to collect auxiliary information such as field maps– are presented and discussed, together with single- and multi-slice *in vitro*, *ex vivo* and *in vivo* MRI comparisons.

Keywords

Ultrafast MRI acquisitions; spatiotemporal encoding; cross-term SPEN; echo-planar imaging

1 Introduction

Nuclear Magnetic Resonance (NMR) finds its widest contemporary application within the context of Magnetic Resonance Imaging (MRI). MRI traditionally retrieves the multidimensional spin density $\rho(\boldsymbol{r})$ being sought by the acquisition of a Free Induction Decay (FID) signal, collected under the action of linear field gradients $\boldsymbol{G} = (G_x, G_y, G_z)$

Corresponding author: Prof. Lucio Frydman, Department of Chemical Physics, Weizmann Institute of Sciences, Phone: +972-8-9344903, FAX: +972-8-9344123, lucio.frydman@weizmann.ac.il.

Author Contributions: ZZ & LF designed research; ZZ & LF performed research; ZZ, AS & LF contributed new tools; ZZ collected data; ZZ, AS & LF analyzed data; LF wrote the paper

Conflicts of Interest: None

Europe PMC Funders Author Manuscripts

acting along orthogonal axes1. Gradients drive the evolution of spins in a reciprocal space $\boldsymbol{k}(t)=\gamma\int_0^t \boldsymbol{G}\left(t'\right)t'$, and the ensuing signal $S(\boldsymbol{k})=\int_{volume}\rho(r)\exp(i\boldsymbol{k}\cdot\boldsymbol{r})d\boldsymbol{r}$ can deliver the information being sought via a Fourier transformation (FT). Out of the alternatives proposed to sample the ***k***-domain supporting these acquisitions, this paper focuses on Mansfield's echo-planar imaging (EPI) proposition,2 an ultrafast approach relying on oscillating the field gradients to monitor sizable ***k***-space volumes in a single shot.3,4 Thanks to its ability to deliver 2D images at a video rate, EPI is the basis of important applications including functional MRI, diffusion-weighted studies and tractography, with applications in both preclinical and human settings5–8. During recent years an alternative ultrafast method has emerged, based on the spatiotemporal encoding (SPEN) of the spin interactions9. Studies have examined the signal to noise, line shapes and relative advantages/disadvantages of SPEN approaches vis-à-vis EPI10–13. The present study introduces an alternative imaging modality that we denominate cross-term SPEN, or xSPEN for short, which in its single-shot implementation presents a most remarkable resilience to field inhomogeneities. While the physical principles of xSPEN will be further detailed below, Figure 1 illustrates its potential with experiments conducted using a variety of pulse sequences under progressively degraded field inhomogeneity conditions. Presented in the top row of this figure are "single-shot" 2D images collected by spin-echo (SE) EPI, SPEN and the new xSPEN sequences under nearly ideal field homogeneity conditions; when compared against a reference image stemming from a robust phase-encoded spin-echo multi-scan experiment, all these results look equally acceptable –with SE-EPI arguably evidencing the best sensitivity for this particular set of acquisition conditions. Degrading the external magnetic field homogeneity rapidly robs EPI from this superiority; for severe enough conditions, the SPEN image also distorts beyond recognition. By contrast the xSPEN scans remain oblivious to the field distortions. *Notably, other than for a FT along the readout dimension and a magnitude calculation of the ensuing matrix, no special processing, field-mapping or additional scans, were associated to the retrieval of these xSPEN images*. The robustness here illustrated is built-in in the raw data acquisition protocol, and derives from xSPEN's new form of delivering NMR images, as further explained below.

2 Results

2.1 Principles of xSPEN in one and multiple dimensions

As starting point for the present discussion, Figure 2a reviews the basis of SPEN MRI. In its 1D implementation this sequence applies a field gradient spreading out the resonance frequencies along an r axis to be imaged, together with a frequency-incremented excitation or inversion radiofrequency (RF) pulse.14,15 Assuming for concreteness the application of a linearly-swept inversion of duration T_p acting while in the presence of an encoding gradient G_{enc} and targeting a field-of-view FOV, this procedure will impose a quadratic spatial encoding on the phases of the spins9, 10

$$\phi_{enc}(r)=\left(-\frac{\gamma G_{enc}T_p}{\mathrm{FOV}}\right)r^2+const. \quad [1]$$

where we have neglected chemical- or susceptibility-derived offsets. Given this dependence and for the usual $\gamma G_{enc} T_p \cdot \mathrm{FOV} \gg 1$ condition, the sole contributors to the observable signal will arise from spins positioned around $r = 0$: for all remaining positions the rapidly varying phase will lead to a destructive interference among neighboring contributions, nulling their macroscopic response. SPEN images are thus read out following the application of a suitable prephasing gradient of area k_{pre} shifting this stationary point to one end of the FOV, and under the action of an acquisition gradient G_{acq} imparting its own $k(t) = \gamma \int_0^t G\left(t'\right) t'$ evolution. Assuming for simplicity a constant G_{acq}, the resulting FID $S(t)$ will then reflect solely those r_0 points fulfilling the time-dependent stationary phase conditions:

$$\left[\frac{\partial\left(\phi_{enc}\left(r\right) + \left(k_{pre} + \gamma G_{acq} t\right) \cdot r\right)}{\partial r}\right]_{r = r_0(t)} = 0. \quad [2]$$

Modulus of the signal collected over an acquisition time $0 \leq t \leq T_a$ ($T_a = 2 G_{enc} T_p / G_{acq}$) will thus be proportional to $\rho(r_0)$. Figure 2a illustrates this non-Fourier image acquisition process, whereby the acquisition gradient rasterizes the sensitive point of the parabola (indicated by a red dot), over the full FOV. Numerous studies have examined the relative merits of this approach vis-à-vis EPI;9–13,16 within the context of this study we remark (i) the potential to extend SPEN to single scan 2D MRI using a so-called "hybrid" approach, whereby an orthogonal axis is encoded by the action of a second, oscillating readout gradient; (ii) the robustness that the ensuing techniques exhibit vis-à-vis field inhomogeneities, susceptibility effects and chemically-derived frequency offsets, thanks from being free of Nyquist-derived EPI gradient constraints; (iii) the additional robustness given to SPEN when performed in a so-called "full refocusing" mode whereby inhomogeneities/shifts are refocused throughout the acquisition process instead of solely at a single spin-echo time17–19; and (iv) the spatial resolution $\Delta r \approx \frac{\partial^2 \phi_{enc}}{\partial r^2}$ of the method, which is related to the curvature of the parabola in Eq. (1) and which can be improved with the help of super-resolution algorithms.20,21

Whereas EPI and SPEN are two options for collecting multidimensional images, there is a third, general approach to obtain arbitrary kinds of 2D NMR correlations. This is the so-called "ultrafast" approach to 2D NMR spectroscopy, which is also based on spatiotemporal principles.22,23 Ultrafast 2D NMR aims to impose in space and in a single shot, the kind of phase pattern that conventional 2D NMR monitors in a time-incremented, multi-scan fashion. Out of the avenues proposed for implementing ultrafast 2D NMR we focus on the constant-time approach illustrated in Figure 2b, involving an initial spin excitation followed by the action of two frequency-swept inversion pulses acting in unison with a pair of bipolar gradients. As explained elsewhere22–25 these manipulations remove the kind of quadratic phase introduced in Eq. (1), and retain solely a bilinear phase encoding that is proportional to both the chemical shifts Ω_i of the targeted sites as well as to their positions r: $\phi_{enc} = C\Omega_i r + \phi_0$, with C a spatiotemporal constant under control (that for this case is $C = 2T_p/\mathrm{FOV}$), and ϕ_0 a phase that is independent of position. Having imposed such an encoding, the application of an acquisition gradient leads to the generation of site-specific gradient echoes whenever

$k(t) = -C\Omega_i$; this principle enables in turn the acquisition of arbitrary n-D (n ≥2) NMR correlations in a single scan.

This spectroscopic-oriented idea could see hitherto untapped extensions into imaging, if the frequencies being encoded would arise from the action of a gradient instead of from discrete chemical shifts; *i.e.,* if Ω were to reflect a position along an axis r_2 (different from the one that is used for imposing the NMR spatiotemporal encoding, which we shall denote r_1) instead of a discrete set of $\{\Omega_i\}$ shifts. Figure 2c illustrates this scenario, for which the encoding considerations will be akin to those just described for the spectroscopic case: $\phi_{enc}(r_1,r_2) = C' r_1 r_2 + \phi_0$, where C' is also a spatiotemporal constant (see Paragraph 2.3 and Supplement 1 for further derivations relating to this expression). The $r_1 r_2$ dependence in ϕ_{enc} differs from the quadratic or linear spatial dependencies deriving from Figures 2a or 2b, in that it involves a product of *two* different spatial variables. We thus refer to it as a cross-term spatiotemporal encoding – "xSPEN" for short. The phase profile of this encoding is also distinct in that it is hyperbolic rather than linear or parabolic, even if like its imaging SPEN counterpart it also possesses a stationary point (indicated in Figure 2c by a red dot) for which $\frac{\partial \phi_{enc}}{\partial r_1} = \frac{\partial \phi_{enc}}{\partial r_2} = 0.$ Also as in the SPEN MRI case this stationary point can be displaced by the action of an acquisition gradient G_{acq}, to rasterize the $\rho(r)$ sample profile. The symmetry of the encoding vis-à-vis two spatial axes, provides a number of different acquisition scenarios. One possibility is to apply the acquisition gradient along the r_1 axis (Fig 2c, option I). As in ultrafast 2D NMR this would reveal the "Ω" spectrum; *i.e.* the image along the r_2 axis, within a projection along r_1 that depends on the width subtended along this axis by the hyperbolic phase. This image formation process can be justified by the fact that the application of an r_1-axis gradient will lead to an observable signal only when the $\left[\frac{\partial\left(\phi_{enc}\left(r_1,r_2\right)+\left(k_{pre}+\gamma G^1_{acq}t\right).r_1\right)}{\partial r_1}\right]_{r_2=(r_2)_0} = 0$ condition is met; 1 this represents a rasterization of the r_2 spatial profile, according to $(r_2)_0(t) = -\frac{k_{pre}}{C'} - \frac{\gamma G^1_{acq}}{C'}t.$ By the same arguments, activating the acquisition gradient along the r_2 axis (option II module in Figure 2c) leads to the SPEN-based acquisition of an image along the r_1 axis. Finally, simultaneous activation of $G^1_{acq}(t)$ and $G^2_{acq}(t)$ gradients over the course of the acquisition leads to a rasterization along a "path" in the (r_1,r_2) plane (Figure 2c, option III module).

Out of the various xSPEN acquisition alternatives, the one highlighted in red on the center-right module of Figure 2c –option II– is particularly intriguing. According to this scheme it is possible to retrieve an image $\rho(r_1)$ by performing a cross-term SPEN encoding, followed by a readout executed by an orthogonally-placed gradient G_2. As G_2 is also part of the encoding process this suggests that it is in principle feasible to perform this $\rho(r_1)$ acquisition, using an orthogonal gradient that is left on continuously. If this were performed as depicted in Figure 2c such imaging sequence would have a few practical shortcomings, including a rasterization that starts at $r_1 = 0$ and a lack of slice selection. Figure 3a presents a refined version of this new approach to 1D MRI scanning, where these technicalities are solved via the inclusion of a free evolution delay $(T_a+p_1)/2$, shifting the hyperbola to the beginning of

the targeted FOV while refocusing the effects of the slice-selective pulse. Notice that these features are implemented by the same orthogonal encoding/decoding gradient, which remains active throughout the course of the scan. Figure 3b illustrates the kind of rasterized, point-by-point image that the ensuing sequence will yield for an idealized 1D profile. While further details on the point-spread-function and resolution considerations for this sequence are presented below, this numerical simulation evidences the method's ability to deliver the desired 1D image.

Given G_2's role as an ancillary gradient whose aim is to help encode and decode positions along r_1, its nature is very different from that of conventional MRI acquisition gradients. Its strength can –within the constraints of the swept-pulse approximations and assumptions underlying the profiles in Figure 2c– be variable. (In practice its value will be chosen low so that the "tightness" of the hyperbola's stationary point along r_2 will exceed the width of the slice selection, minimize eventual diffusion losses, and reduce the RF power requirements.) Even the gradient's physical geometry –its orientation, linearity, or uniaxial purity– are secondary to the physics of the image formation process. Indeed, if instead of a linear 1D gradient G_2 causing a spreading of the resonance frequencies over a range $\Delta\omega = \gamma G_2 \mathrm{FOV}_2$ one would deal with a different kind of frequency broadening –for instance one originating from a complex spatial dependence like that associated to B_0 field heterogeneities, one arising from various discrete isotropic chemical shifts acting on top of a field gradient, or an intrinsic orientation-dependent NMR anisotropy– the acquisition principles summarized in Figures 3a and 3b, would not change. What would change is the nature of the "$G(r_2)$", which instead of being correlated one-to-one with a physical axis, would become a generic $\Delta\omega$ line broadening. The method's point spread function (PSF) would then deviate from the idealized *sinc*-like form assumed in Figure 3, and the details of the slice-selection pulse would be affected –but not the principles of xSPEN's encoding and decoding of the $\rho(r_1)$ spatial profile. From these considerations it follows that *if instead of involving an ideal field gradient, the frequency-dispersing mechanism involves a gradient superimposed on other sources affecting the spins' rates of precession –for instance dispersions over multiple chemical shifts, substantial susceptibility effects or 3D field-derived broadenings– the appearance of the collected xSPEN image will not be significantly altered.* Indeed in such cases spins in different voxels would be excited/inverted by the pulses at times that do not correspond to their ideal expectation; but these miss-timings would cancel out with miss-timings in the formation of the spatial "r_2-echo", so that the timing of ρ's rasterization during the course of the acquisition reinstates all r_1-values to their ideal locations. This voxel-by-voxel cancelation of arbitrary non-idealities in timing and in accrued phases does not require any *a priori* knowledge or any special post-processing, and it is what endows the xSPEN images illustrated in Figure 1 with their capabilities to withstand very large field inhomogeneity effects. A more detailed derivation of these effects and of their image-leading behavior, is presented in Supplement 1.

2.2 Single-scan 2D xSPEN: Comparative examples

An area of contemporary MRI where field inhomogeneities remain an important challenge, is that of single-shot experiments. As mentioned, EPI is currently a method of choice for functional, diffusion and other MRI studies requiring fast scanning; but it is usually much

more sensitivity to field distortions than multi-scan MRI –particularly along its blipped, low-bandwidth dimension. Figure 3c illustrates how the 1D xSPEN approach just described, can be extended to perform single-scan 2D acquisitions. This sequence is just one of several alternatives that can be conceived for 2D single-shot acquisitions (see Supplement 3 for further xSPEN options), and it incorporates an oscillating readout gradient monitoring one of the axes conjugate *k*-space (which for simplicity we call *x*), and the application of a constant gradient (previously called r_2, which we now associate to G_z) for both slice selection and for rasterizing the second domain (r_1, now assigned to the *y*-axis). For completion Figure 3d illustrates how these oscillating and constant gradients transverse the resulting "hybrid" (k_x,*y*) space. All that such sequence needs –and what was implemented in the present study– to transform the $S(t)$ sampled during the acquisition into the xSPEN images introduced in Figures 1 and 4-6, is to splice the resulting 1D FID string into $\pm G_{ro}$-sampled segments, position these in their correct 2D space coordinates, subject these rearranged arrays to a 1D FT *vs* k_x, and display in magnitude-mode the resulting matrix.

As further illustration on the resilience of this new method to offsets, Figure 4 presents results collected on a phantom incorporating two features that are notoriously challenging to single-shot acquisitions: a titanium screw of the kind used in orthopedic implants, and a sample composed of several and nearly equipopulated, chemically-shifted sites. Glued to the titanium screw was a Lego® piece of characteristic shape (Figure 4a), centered within a 30 mm diameter tube holding the sample. Figure 4b illustrates six NMR spectra acquired for corresponding slices positioned along the axis of the tube. Although the three main resonances of the sample can be recognized in all these PRESS-selected slices the metal-induced field distortions are also evident, with line widths varying between 70 and 250 Hz, depending on position. Figures 4c-4f illustrate images arising from the same six slices, using a variety of pulse sequences. The multi-scan SE data shown in Figure 4c provides the reference images, thanks to the small values of the distortions and chemical shifts vis-à-vis the bandwidth (250 kHz) used in this experiment's acquisition dimension. The multi-site nature of the sample prevents the acquisition of clear EPI images even in homogeneous field regions, and even less so in slices where the field is affected by the titanium screw (Figure 4d). These severe distortions reflect the low bandwidth (~2.9 kHz) that can be activated in this SE-EPI scan along the phase encoding dimension; even the collection of blip-less "navigator" scans,26,27 fail to provide the information needed to suppress the metal- and shift-derived artifacts. The conventional SPEN images (Figure 4e) present a more robust alternative: chemical shift artifacts are reflected mostly as minor stripes (best observable in the z_0 = -1.5, -0.9 cm slices that are largely devoid from metal-derived artifacts) thanks to the sequence's fully-refocused character. Also the spatially-dependent titanium-derived artifacts are remarkably smaller than in their EPI counterparts thanks to the ~13.6 kHz acquisition bandwidth that can be accommodated along the SPEN axis (given by the average G_{acq} times the FOV_y). Still, slices encompassing the titanium screw lead to distorted images. By contrast, xSPEN-derived images are –apart from sensitivity considerations dictated by their much smaller number of averaged transients– virtually indistinguishable from those arising from the multi-scan counterparts. This, despite of the fact that the whole xSPEN set was acquired within 360 ms (60 ms per slice, no relaxation delays within slices, no need for navigator scans or field maps) with only a 2.9 kHz effective bandwidth along the xSPEN

dimension. Interestingly, even some of the minor artifacts arising in the xSPEN images mirror one-to-one similar artifacts observable in the multi-scan counterparts. As discussed in Supplement 1, these distortions do not arise from chemical shift or field inhomogeneity effects along the low- or high-bandwidth dimensions, but rather from non-uniformities in the thickness and flatness of the slices excited by the selective pulses initiating all these sequences. The sole notable xSPEN-specific artifacts are a slight coarseness and a signal decay along the *y*-axis, reflecting a slightly lower resolution and the effects of the decoherence over the course of the signal acquisition.

Figure 5 demonstrates further the potential of this new kind of experiments, with *in vivo* single-shot acquisitions performed on mice in a 7 T magnet. Due to the relatively narrow bore (120 mm) of this system, shimming capabilities were limited to ≥40 Hz line widths over 4x10x10 mm^3 volumes; as a result, quality EPI images could only be recorded from the brain's central region. Three planes were acquired using multi-scan SE as well as single-shot SE EPI, SPEN and xSPEN sequences, including coronal and sagittal images along the length of the animal's head. When applied to the selected head region, the multi-scan image acting as reference (Figure 5a, top) shows clearly the mouse's eyes, brain and snout. Due to field susceptibility effects, however, certain regions –particularly the eyeballs– appear severely distorted in SE EPI, and somewhat distorted in the SPEN experiments (Figure 5b and c). Fat artifacts are also evident in these single-shot images –all of which were recorded without fat suppression. By contrast the single-scan xSPEN images are free from any evident distortions and, apart from SNR considerations, comparable one-to-one to their multi-scan counterparts. The success of xSPEN is further evidenced in the coronal and sagittal slices, which reproduce faithfully both the eyes and ears regions. In fact, given that all these experiments were collected without an external respiratory trigger, certain motion artifacts can be noticed in the coronal and sagittal planes of the lengthier multi-scan SE experiments along their phase-encoded dimensions, which are absent in the single-shot xSPEN scans.

Notwithstanding the relatively long inversion pulses that it involves, the xSPEN sequence in Figure 3c shows an efficient multi-slicing performance. This stems from its reliance on an initial slice-selective pulse, followed by an encoding with a pair of frequency-swept π pulses. Such pair of inversions can act with remarkably efficiency even in the presence of field inhomogeneities;29 multi-slicing can thus be repeated in rapid succession despite the wide slabs that these inversion pulses address. Subtleties will still be involved in xSPEN multislicing owing to the use of slice selection while under the action of a G_z gradient, followed by the action of swept pulses while under the action of $G_z \pm G_y$ gradient combinations. As further explained in Supplement 2 this may complicate the collection of slices with zero inter-slice separation; still, 2D images separated by small gaps could routinely be acquired. This ability is illustrated by the *in vivo* mouse head coronal images shown in Figure 6. The overall line width of the ^{1}H resonance in the targeted volume was ca. 120 Hz; under such conditions the susceptibility and other static field B_0 homogeneity distortions simply precluded the acquisition of SE EPI images in all but the center region of the brain. As in Figure 5, also here the lack of respiratory synchronization robs navigator scans from much of their usefulness, leading to artifacts along SE-EPI's phase-encoded dimension. The higher bandwidth and fully-refocused character of SPEN provides an enhanced immunity against all these artifacts; still, even in this case, images are clearly

biased in regions proximate to air/tissue interfaces subject to the largest susceptibility distortions. By contrast, the xSPEN images are nearly identical to the multi-scan references for all the slices, despite the sub-second nature of this volumetric measurement. Notice as well that in this case, the fact that fat suppression is not utilized has only a marginal effect on the single-shot images.

2.3 Sampling, resolution, FOV and signal-to-noise considerations

Figures 1 and 4-6 illustrate the potential of xSPEN. This paragraph derives some basic characteristics of this imaging modality under idealized conditions; *i.e.*, in the absence of field inhomogeneities, chemical shifts or relaxation effects. Most of these features can be gathered by deriving the spin evolution arising in the sequence. Following similar definitions as those employed in the derivation of SPEN MRI,10,24 the phase evolved by the spins following the action of the swept pulses plus the $T_a/2$ free evolution delay in-between them, can be described as

$$\phi_{enc}(y,z) = -Cy \cdot \gamma G_z z - \gamma G_z z \cdot \frac{T_a}{2}, \quad [3]$$

where $C = \frac{4T_p \gamma G_y}{2\pi BW}$, and the initial excitation pulse's dephasing has been accounted for by the additional $p_1/2$ delay in-between the sweeps. C is here defined using the chirp bandwidth BW of the pulses rather than the sample's length as in previous works, given that these sweeps will now happen along tilted axes fulfilling $BW = |\gamma G_z L_z| + |\gamma G_y FOV_y|$. Notice as well that whereas in this expression FOV_y will be the targeted imaging region, L_z is a region on the order of the slice-selected thickness (assumed centered at zero) over which the y-imaging acquisition will be supported. Following this initial encoding, acquisition of an FID in the presence of a gradient of the same magnitude G_z, carries out an analog Fourier transformation

$$S(t) \propto \int_Y \left[\int_{-L_z/2}^{L_z/2} dz \rho(y,z) \cdot e^{i\phi_{enc}(y,z)} e^{i\gamma G_z t z} \right] dy, \quad [4]$$

Assuming for simplicity that the z-dependence of the image within the slice is weak enough to be disregarded, this leads to

$$S(t) \propto \int_Y \left[\int_{-L_z/2}^{L_z/2} dz \rho(y) \cdot e^{i\left[-Cy - \frac{T_a}{2} + t\right]\gamma G_z z} \right] dy \quad [5a]$$

$$= \int_Y dy \rho(y) \cdot L_z \mathrm{sinc}\left\{ \left[-C'y + k(t) \right] \cdot \frac{L_z}{2} \right\} \quad [5b]$$

where we have defined as the acquisition wavenumber $k(t) = \gamma G_z(t\text{-}T_a/2)$ and $C' = C\gamma G_z$. Equation [5b] predicts that the signal collected as a function of an acquisition time $0 \leq t \leq T_a$ will be the convolution of the $\rho(y)$ image being sought, with a *sinc* function displacing throughout the acquisition and highlighting at each moment y-coordinates fulfilling

$$y(t)=\frac{k(t)}{C'}=\frac{\gamma G_z(t-T_a/2)}{C\gamma G_z}=\frac{2\pi BW}{4T_p\gamma G_y}\cdot(t-T_a/2)\ . \quad [6]$$

This increment in the *sinc's* maximum, illustrated by the propagating colored functions in Figure 3c, is analogous to the increment of conventional SPEN's stationary phase point with time. As xSPEN's imaging point spread function is given by this *sinc* function, the ensuing spatial resolution can thus be defined by this function's half-height width

$$\delta y=\frac{2\pi FOV_y}{T_a\cdot\gamma G_z L_z}=\frac{\pi^2 BW}{\gamma G_y\cdot\gamma G_z L_z\cdot T_p}. \quad [7]$$

Notice that as in conventional SPEN, resolution in xSPEN can be improved by increasing the duration of the T_p frequency-swept encoding pulses or, as in ultrafast NMR, by enlarging the "support" L_z. As for the actual FOV that this *sinc* function will raster along the imaged axis, this will be given by the duration over which the k-wavenumber will be allowed to act; for a suitable setting one would demand $\mathrm{FOV}_y = |k_{\max} - k_{\min}|/C' = \gamma G_z T_a/C'$.

It is instructive to compare the SNR that, under comparable FOV_y and δy conditions, will arise from xSPEN vis-à-vis a conventional k-based method like EPI. SNR is defined as a ratio between a mean signal intensity (s_{mean}) and the root-mean-square of a statistically random noise n_{rms}. Under the assumption just made the voxel sizes will be equal for both imaging modalities, and similar time-domain signals s_{mean} will arise. The random noise will be mainly dictated by the bandwidth requirements of the readout dimension; once again, this will be similar for xSPEN and EPI experiments. Still, the FT that would benefit a k-space method like EPI with a $\sqrt{N_{\mathrm{Acq}}}$ enhancement, reflecting the multiplexing advantage associated to the sampling of N_{acq} points, will be absent in the raw magnitude-mode processing illustrated here for xSPEN. This implies that

$$\frac{SNR^{(\mathrm{xSPEN})}}{SNR^{(\mathrm{EPI})}}=\frac{1}{\sqrt{N_{Acq}}}=\sqrt{\frac{\delta y}{\mathrm{FOV}_y}}=\sqrt{\frac{2\pi}{T_a\cdot\gamma G_z L_z}}. \quad [8]$$

For the parameters used in this study, this amounts to a severe loss in SNR vis-à-vis EPI. This can actually be appreciated from the results shown in Figure 1, where both EPI and SPEN have better SNR than xSPEN under homogeneous field conditions. As soon as inhomogeneities and non-idealities take over, however, xSPEN's fidelity more than compensates for this SNR penalty. It is also worth remarking that while initial SPEN

implementations also suffered from a similar $\sqrt{N_{\mathrm{Acq}}}$ reduction in SNR compared to Fourier imaging;9 this penalty was eventually removed by the use of super-resolution algorithms.12 Similar algorithms might help the xSPEN case as well.

3 Discussion and Conclusions

The arguments and results in the preceding Sections demonstrate the potential of cross-term spatiotemporal encoding. Highlighted in particular was the method's unprecedented robustness to a variety of field heterogeneities, including those arising from magnetic susceptibility effects, from multiple chemical shifts, and from global static field inhomogeneities. To highlight this immunity we focused on single-shot imaging implementations, whose phase-encoded domains are notoriously sensitive to field distortions. The xSPEN approach then evidenced fewer distortions than any single-shot counterpart; in fact, careful tests reveal that xSPEN is often more resilient to inhomogeneities –and certainly to motion– than even multi-scan spin-echo counterparts (see for instance xSPEN's reduced distortions evidenced by the bottom images of Figure 1). This could make xSPEN an ideal tool for tackling certain challenging MRI investigations including: studies of organs with substantial tissue/air interfaces; scans suffering from motional distortions in abdominal regions or in fetal investigations; real-time cardiac and musculoskeletal measurements; diffusion-oriented studies; scans in proximity to metallic tools of the kind used in surgical procedures or ultrasound ablation; dealing with organs where fat suppression can be challenging; single-sided MRI investigations liable to large uni-dimensional field distortions; ultrahigh field imaging; and even –as illustrated in Supplement 5– the imaging solid-like objects. Moreover, the built-in "zooming" capabilities that the swept pulses endow xSPEN with, provide excellent starting points for simpler applications, like rapid scouting of organs in inhomogeneous regions or in low-cost magnet systems. The potential of these various proposals, as well as extensions of xSPEN to multi-shot investigations of the kind exemplified in Supplement 4, are being explored in both preclinical and clinical settings.

Notwithstanding the versatility and benefits evidenced by xSPEN MRI, a number of issues remain to be solved. One of these is the SNR penalty treated earlier; we are looking into signal processing alternatives to alleviate this. An additional penalty arises from the progressive nature of the image acquisition, which due to relaxation and diffusion effects will be associated to position-dependent losses. Such distortions were noticed along the phase-encoded axes of Figure 4, and although they can be attenuated by reducing the swept pulses and acquisition times, this will come at the expense of some spatial resolution; alternative routes to cope with this are being explored. Finally, practical complications may also arise from the high specific-absorption-rate (SAR) that in human scanners might result from the use of dual frequency-swept π-pulses, or from the gap between slices that will often arise in the multi-slice implementations of the xSPEN experiments. Experiments to evaluate the importance and minimize the relevance of these problems, are also under investigation.

Europe PMC Funders Author Manuscripts

4 Methods

All acquisitions were carried out on a 7T/120mm horizontal magnet MRI using a quadrature birdcage coil probe (Agilent Technologies, Santa Clara, CA). The spin-echo multi-shot (SEMS) imaging and the point-resolved (PRESS) localized spectroscopy experiments, were carried out using sequences taken from the scanner's software libraries. SPEN and xSPEN imaging experiments were run using macros that were fully integrated into the Agilent/Varian VNMRJ® imaging systems. These automated programs enable numerous options such as selecting a zoomed region of interest, performing a pre-scan gradient calibration, arbitrary single- or multi-slicing, arraying of parameters, water/fat suppression, automatic TE and TR minimization, etc. The installation package also incorporates referenceless on-the-fly reconstructions –including SPEN's referenceless super-resolution data processing30– that are compatible with various post-processing tools of the native VNMRJ environment. Such packages are available upon request.

The parameters used for setting up the various experiments were detailed in the corresponding figures' captions. In general they included: matrix size = 64 × 64; acquisition bandwidth = 250 kHz; FOV = 40 × 40 × 3 mm^3 for the Lego® phantom acquisitions; FOV = 40 × 40 × 4 mm^3 for the *ex vivo* acquisitions; FOV = 25 × 25 × 4 mm^3 for the axial *in vivo* single-slice acquisition; FOV = 30 × 40 × 3 mm^3 for the *in vivo* coronal and sagittal single-slice acquisitions; FOV = 30 × 60 × 3 mm^3 for the *in vivo* multi-slice coronal acquisitions. Interslice gaps were 3 mm for the multi-slice phantom acquisitions and 1 mm for the multi-slice *in vivo* acquisitions. Swept-pulse bandwidths and durations in the SPEN experiments were set to 13.6 kHz and 11.01 ms respectively, while for the xSPEN experiments these were 5.8 kHz and 11.01 ms. For the xSPEN experiments G_z was set to 2.28 or 1.71 G/cm depending on whether a slice thickness of 3 or 4 mm was used, respectively. G_y was set to 0.27 or 0.17 or 0.114 G/cm, for xSPEN FOVs along *y* axis of 25 or 40 or 60 mm, respectively. The time needed for scanning each slice in either SPEN or xSPEN experiments was about 60 ms; for EPI acquisitions the single-shot duration was the same, but the scanner required ca. 2 s when including the acquisition of reference "navigator" scans. All SE multi-shot acquisitions required 2 m 8 s. Animal protocols and maintenance were done in accordance with guidelines of the Institutional Committee on Animals of the Weizmann Institute of Science (IACUC protocol 10790514).

Supplementary Material

Refer to Web version on PubMed Central for supplementary material.

Acknowledgments

We are grateful to Dr. Nava Nevo (WIS Veterinary Services) for the rat brain specimens, and to Koby Zibzener for assistance in the acquisition of the experiments. This work was funded by the Israel Science Foundation grant 795/13, by ERC-2014-PoC grant # 633888, by the Kimmel Institute of Magnetic Resonance, and by the generosity of the Perlman Family Foundation. ZZ is thankful for financial support from the China Scholarship Council (201306310056).

Abbreviations

EPI	Echo-Planar Imaging
FID	Free Induction Decay
FT	Fourier transform
FOV	Field of View
MRI	Magnetic Resonance Imaging
NMR	Nuclear Magnetic Resonance Spectroscopy
PRESS	Point-Resolved Spectroscopy
RF	Radiofrequency
SE	Spin-echo
SNR	Signal-to-Noise ratio
SPEN	SPatiotemporal ENcoding
xSPEN	Cross-term SPatiotemporal ENcoding

References

1. Bernstein, MA., King, KF., Zhou, XJ. Handbook of MRI Pulse Sequences. Elsevier Academic Press; 2004.
2. Mansfield P. Multi-planar image-formation using NMR spin echoes. J Phys C: Solid State Phys. 1977; 10:L55–L58.
3. Stehling MK, Turner R, Mansfield P. Echo-planar imaging: magnetic resonance imaging in a fraction of a second. Science. 1991; 254:43–50. [PubMed: 1925560]
4. Schmitt, F., Stehling, MK., Turner, R. Echo-planar imaging: theory, technique and application. Springer; 1998.
5. Turner R, et al. Echo-planar imaging of intravoxel incoherent motion. Radiology. 1990; 177:407–414. [PubMed: 2217777]
6. Ugurbil K, et al. Ultrahigh field magnetic resonance imaging and spectroscopy. Magn Reson Imaging. 2003; 21:1263–1281. [PubMed: 14725934]
7. van der Zwaag W, et al. Temporal SNR characteristics in segmented 3D-EPI at 7T. Magn Reson Med. 2012; 67:344–352. [PubMed: 21656557]
8. Norris DG. Spin-echo fMRI: The poor relation? Neuroimage. 2012; 62:1109–1115. [PubMed: 22245351]
9. Shrot Y, Frydman L. Spatially encoded NMR and the acquisition of 2D magnetic resonance images within a single scan. J Magn Reson. 2005; 172:179–190. [PubMed: 15649744]
10. Tal A, Frydman L. Single-scan multidimensional magnetic resonance. Prog Nucl Magn Reson Spectrosc. 2010; 57:241–292. [PubMed: 20667401]
11. Goerke U, Garwood M, Ugurbil K. Functional magnetic resonance imaging using RASER. Neuroimage. 2011; 54:350–360. [PubMed: 20699123]
12. Ben-Eliezer N, Shrot Y, Frydman L, Sodickson DK. Parametric analysis of the spatial resolution and signal-to-noise ratio in super-resolved spatiotemporally encoded (SPEN) MRI. Magn Reson Med. 2014; 72:418–429. [PubMed: 24136737]

13. Li J, et al. Imaging with referenceless distortion correction and flexible regions of interest using single-shot biaxial spatiotemporally encoded MRI. Neuroimage. 2015; 105:93–111. [PubMed: 25462700]
14. Kunz D. Use of frequency-modulated radiofrequency pulses in MR imaging experiments. Magn Reson Med. 1986; 3:377–384. [PubMed: 3724417]
15. Pipe JG. Spatial encoding and reconstruction in MRI with quadratic phase profiles. Magn Reson Med. 1995; 33:24–33. [PubMed: 7891532]
16. Tal A, Frydman L. Spatial encoding and the single-scan acquisition of high definition MR images in inhomogeneous fields. J Magn Reson. 2006; 182:179–194. [PubMed: 16843690]
17. Chamberlain R, et al. RASER: A new ultrafast magnetic resonance Imaging method. Magn Reson Med. 2007; 58:794–799. [PubMed: 17899612]
18. Ben-Eliezer N, Shrot Y, Frydman L. High-definition, single-scan 2D MRI in inhomogeneous fields using spatial encoding methods. Magn Reson Imaging. 2010; 28:77–86. [PubMed: 19608367]
19. Schmidt R, Frydman L. New spatiotemporal approaches for fully refocused, multislice ultrafast 2D MRI. Magn Reson Med. 2014; 71:711–722. [PubMed: 23468061]
20. Ben-Eliezer N, Irani M, Frydman L. Super-resolved spatially encoded single-scan 2D MRI. Magn Reson Med. 2010; 63:1594–1600. [PubMed: 20512863]
21. Cai C, et al. An efficient de-convolution reconstruction method for spatiotemporal-encoding single-scan 2D MRI. J Magn Reson. 2013; 228:136–147. [PubMed: 23433507]
22. Frydman L, Scherf T, Lupulescu A. The acquisition of multidimensional NMR spectra within a single scan. Proc Natl Acad Sci U S A. 2002; 99:15858–15862. [PubMed: 12461169]
23. Frydman L, Lupulescu A, Scherf T. Principles and features of single-scan two-dimensional NMR spectroscopy. J Am Chem Soc. 2003; 125:9204–9217. [PubMed: 15369377]
24. Pelupessy P. Adiabatic single scan two-dimensional NMR spectroscopy. J Am Chem Soc. 2003; 125:12345–12350. [PubMed: 14519020]
25. Shrot Y, Frydman L. Spatial encoding strategies for ultrafast multidimensional nuclear magnetic resonance. J Chem Phys. 2008; 128
26. Butts K, deCrespigny A, Pauly JM, Moseley M. Diffusion-weighted interleaved echo-planar imaging with a pair of orthogonal navigator echoes. Magn Reson Med. 1996; 35:763–770. [PubMed: 8722828]
27. Mori S, van Zijl PC. A motion correction scheme by twin-echo navigation for diffusion-weighted magnetic resonance imaging with multiple RF echo acquisition. Magn Reson Med. 1998; 40:511–516. [PubMed: 9771567]
28. Kupce E, Freeman R. Stretched adiabatic pulses for broadband spin inversion. J Magn Reson, Ser A. 1995; 117:246–256.
29. Garwood M, DelaBarre L. The return of the frequency sweep: designing adiabatic pulses for contemporary NMR. J Magn Reson. 2001; 153:155–177. [PubMed: 11740891]
30. Seginer A, Schmidt R, Leftin A, Solomon E, Frydman L. Referenceless reconstruction of spatiotemporally encoded imaging data: principles and applications to real-time MRI. Magn Reson Med. 2014; 72:1687–1695. [PubMed: 24420445]
31. Shrot Y, Shapira B, Frydman L. Ultrafast 2D NMR spectroscopy using a continuous spatial encoding of the spin interactions. J Magn Reson. 2004; 171:163–170. [PubMed: 15504696]
32. Andersen NS, Kockenberger W. A simple approach for phase-modulated single-scan 2D NMR spectroscopy. Magn Reson Chem. 2005; 43:795–797. [PubMed: 16007727]
33. Tal A, Shapira B, Frydman L. A continuous phase-modulated approach to spatial encoding in ultrafast 2D NMR spectroscopy. J Magn Reson. 2005; 176:107–114. [PubMed: 15949960]
34. Schmidt-Rohr, K., Spiess, HW. Multidimensional solid-state NMR and polymers. Academic Press; 1994.

Europe PMC Funders Author Manuscripts

Significance Statement

MRI in general, and particularly single-scan MRI, has been hitherto constrained to acquisitions in high quality magnets. The present study introduces a methodology that can deliver such images under much poorer external field conditions. These capabilities are achieved based on new principles whereby images are read using field gradients that are not applied along the direction being encoded. This enables one to accommodate large inhomogeneities into the single-scan image acquisition protocol, without suffering from miss-registrations, without requiring *a priori* information for post-acquisition corrections, or without demanding specialized instrumentation. This can thus enable investigations that have hitherto escaped from MRI's scope, including the fast scanning of brain regions suffering from strong tissue/air susceptibility problems, scans in brain and spine regions close to metal implants, real-time imaging of limbs in open magnets, fast MRI in the presence of metallic tools as usually present in surgery rooms, and acquisitions in otherwise low-quality magnets.

Europe PMC Funders Author Manuscripts

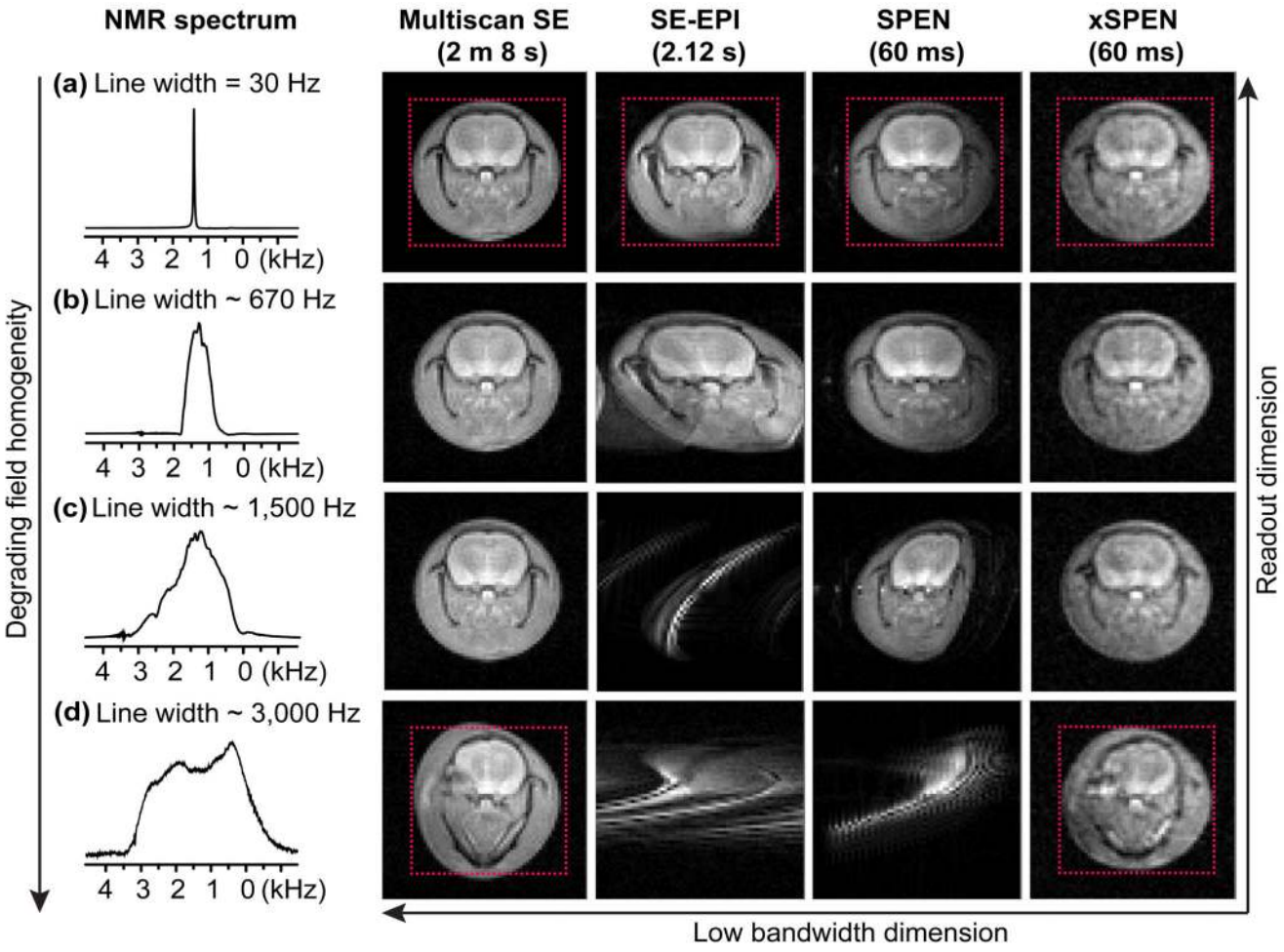

Figure 1.

Ex-vivo rat brain 1D NMR and 2D imaging results from different sequences, collected for increasingly degraded magnet field homogeneity conditions. (a) 1D spectrum and images acquired using multi-scan SE, SE-EPI, SPEN and xSPEN sequences, in a uniform magnetic field where the water resonance is characterized by a 30 Hz full width at half maximum. (b, c, d) Idem but acquired in magnetic fields that were deliberately and arbitrarily deteriorated, as evidenced by the increasing 1D NMR half-height line widths mentioned on the left-hand column. Notice the progressive distortions introduced by the field inhomogeneity in all images but the xSPEN one, as judged by the dotted squares added for ease of viewing. Remarkably, for the largest inhomogeneities, distortions are more noticeable for the multi-scan reference image than for the xSPEN counterpart. Common scan parameters: FOV = 40 × 40 mm^2; slice thickness = 4 mm; matrix size = 64 × 64; acquisition bandwidth = 250 kHz; slice selection pulse gradient = 1.71 G/cm (kept constant for all sequences and conditions). Repetition time TR = 2 s for the multi-scan SE and EPI sequences; TR = 60 ms for the SPEN and xSPEN sequences. The 1D peaks correspond to point-resolved (PRESS) NMR spectra collected on the same FOVs as the 2D images. The extended acquisition time of the EPI scan reflects the need for an ancillary navigator scan, which is not needed/used by any of the SPEN experiments. Additional parameters: sweep bandwidth = 13.6 kHz and sweep

duration = 11.01 ms for SPEN; sweep bandwidth = 5.8 kHz and sweep duration =11.01 ms for xSPEN. Also used in the latter were a constant G_z gradient = 1.71 G/cm and an encoding G_y gradient = 0.17 G/cm. See text and Figure 3c for further details.

Europe PMC Funders Author Manuscripts

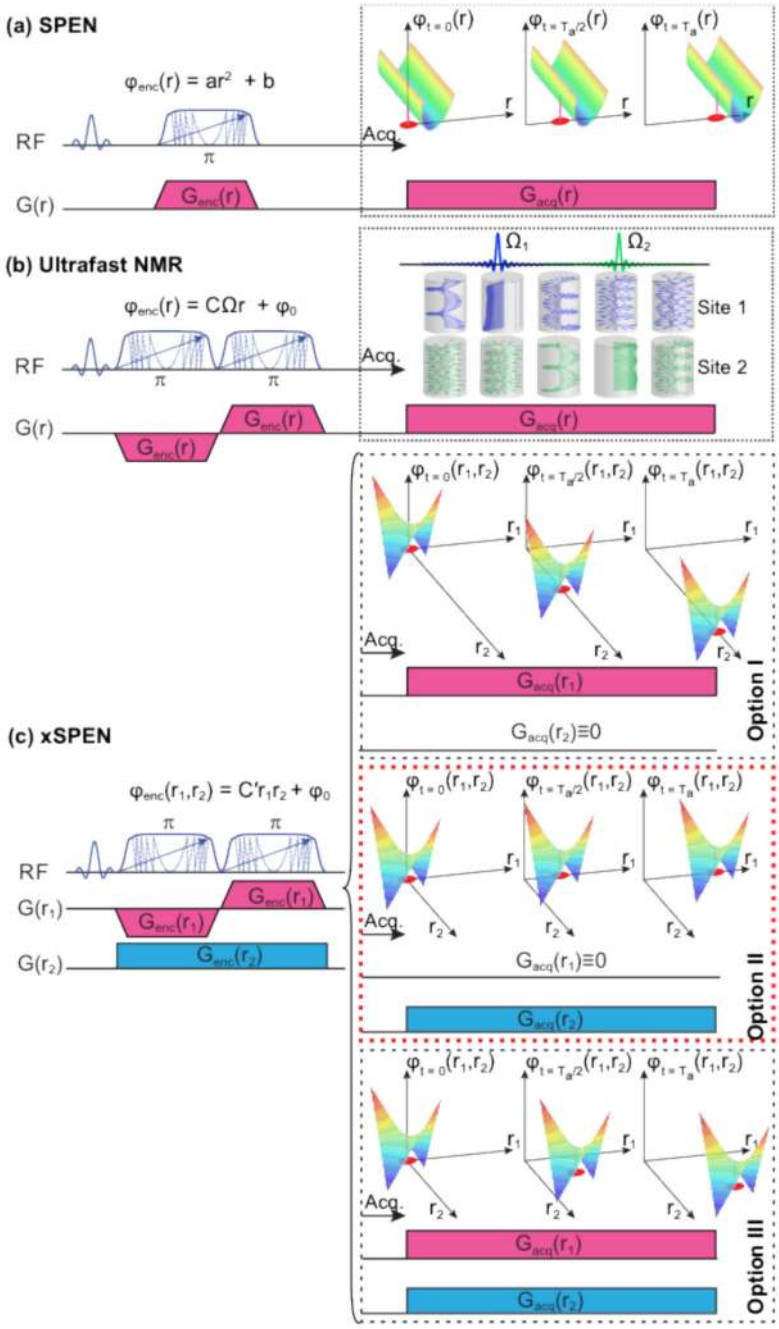

Figure 2.

Spatiotemporal encoding approaches. (a) The SPEN imaging approach, imparting a parabolic phase on the spins along an axis r by applying a linearly swept inversion pulse under the action of an r-axis gradient; during the acquisition, the stationary point (which in this 2D case will actually be a line) moves along r axis driven by $G_{acq}(r)$. (b) Ultrafast 2D NMR spectroscopy, where N discrete frequencies to be read are spatially encoded via frequency-swept inversion pulses acting under the action of a bipolar gradient. This leads to magnetizations wound by phase terms $\{C\Omega_i r\}_{i=1..N,}$ whose frequencies can be read out as

site-specific echoes emerging upon applying a continuous $G_{acq}(t)$. (c) The xSPEN MRI approach, where an ultrafast-like sequence involving two swept pulses in the presence of a bipolar gradient $G_{enc}(r_1)$, are used to encode positions thanks to the action a second gradient $G_{enc}(r_2)$. This dual-axis encoding leads to a hyperbolic phase profile in the (r_1,r_2)-plane possessing, like SPEN, a stationary point (red dot). During the data acquisition process, the position of this stationary point can be shifted along the r_2 axis by the application of an r_1-axis gradient (c, option I) or along r_1 by the action of an r_2-axis gradient (c, option II). Other scanning options could also be envisioned (c, option III).

Europe PMC Funders Author Manuscripts

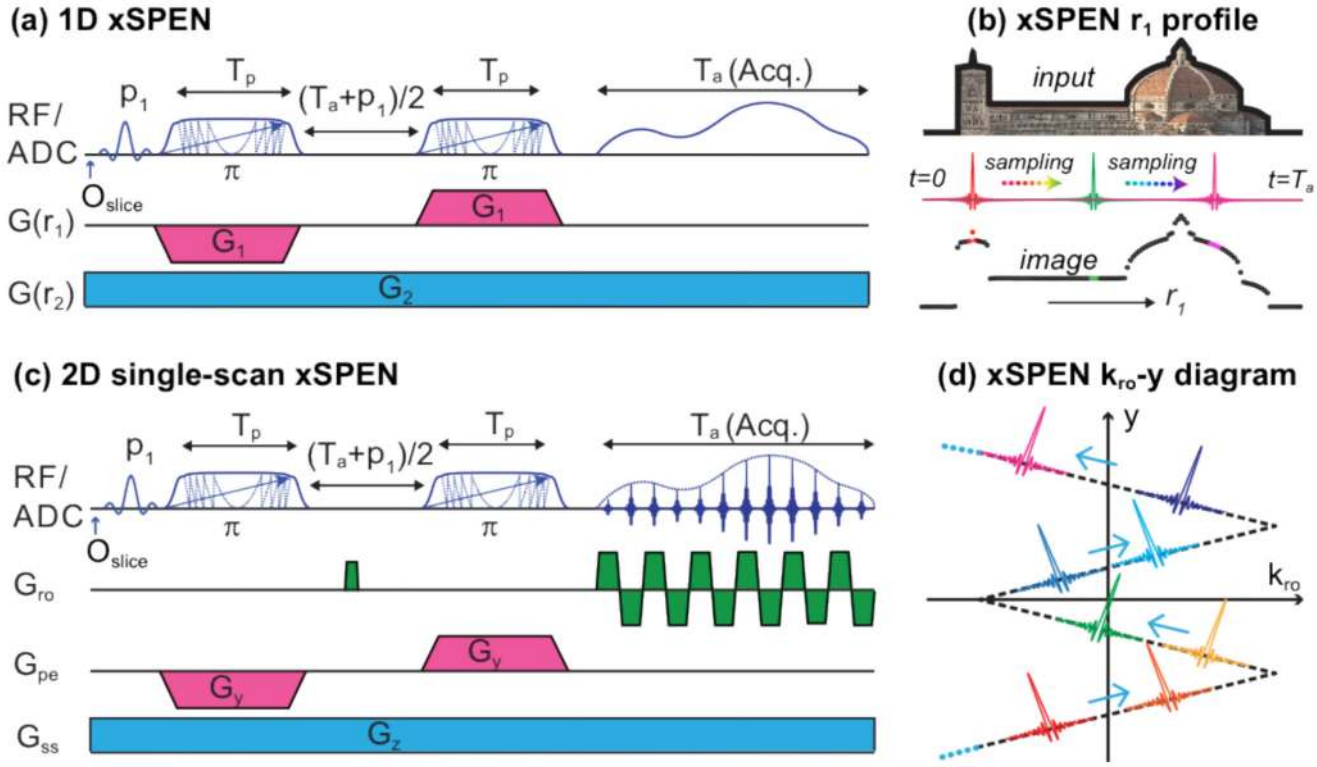

Figure 3.

Expanding the xSPEN's principles to sequences that are highly immune to field inhomogeneity distortions. (a) 1D version incorporating a constant G_2 gradient associated with slice-selecting and with encoding/decoding the $\rho(r_1)$ image. (b) r_1-profile delivered by sequence (a) on the illustrated input, equivalent to the landscape trace convoluted with a *sinc* sampling function that displaces over the course of the data acquisition –no FT being involved in the $\rho(r_1)$ image formation. (c) Extending the 1D xSPEN concept to a single-scan 2D sequence, incorporating an oscillating *k*-based gradient encoding along *x* and an xSPEN-based rasterization of *y*-profiles by means of a *z* gradient. (d) Sampling of the k_x-*y* space delivered by the hybrid 2D xSPEN sequence in (c).

Europe PMC Funders Author Manuscripts

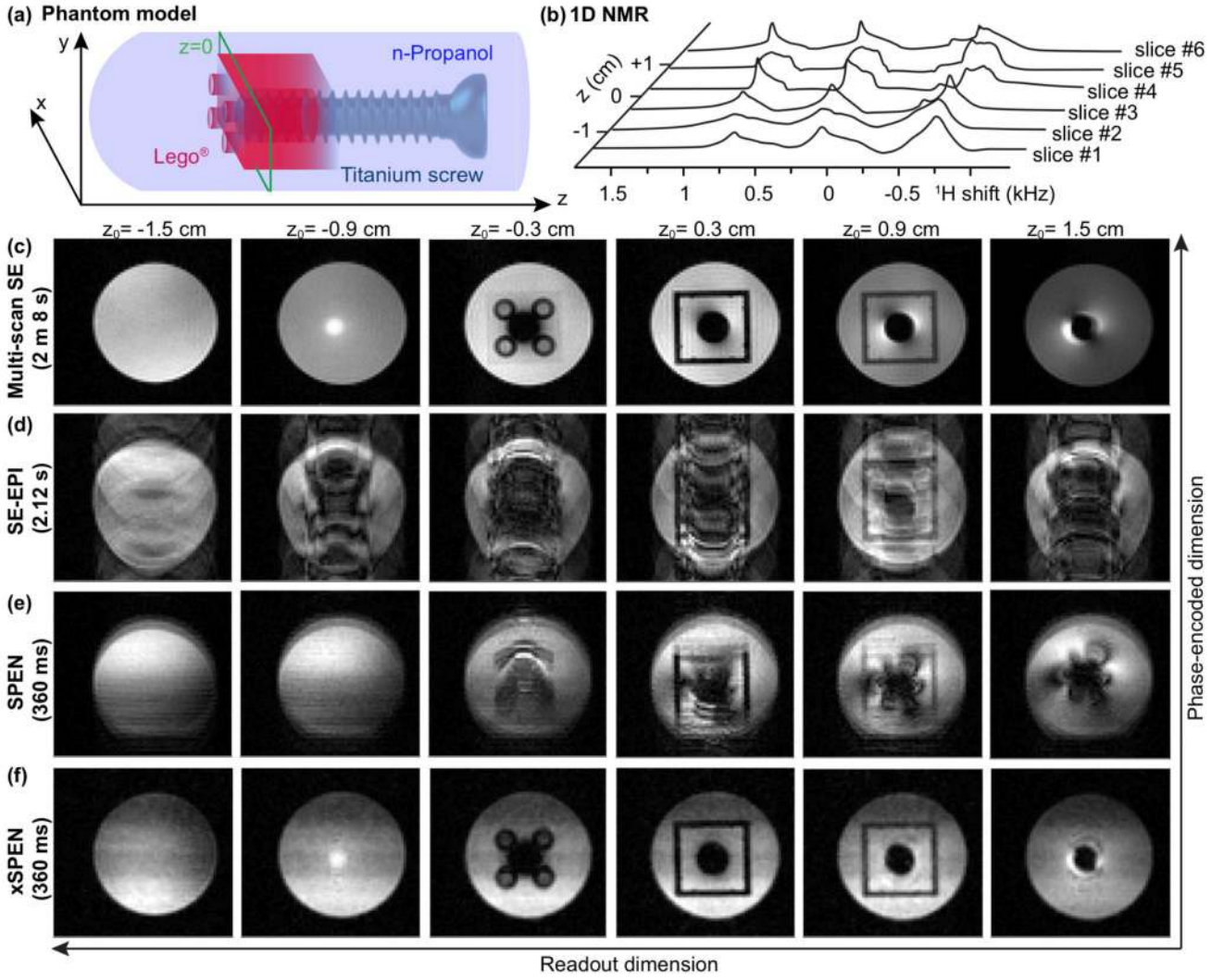

Figure 4.

Comparing the performance of various 2D multi-slice sequences. (a) Cartoon of the targeted phantom made up of a Lego® block glued to a central titanium screw, immersed in a tube filled with n-propanol. Also indicated is the approximate $z = 0$ position. (b) 1D NMR spectra acquired from six slices at the indicated positions, using PRESS. (c, d, e, f) Images arising from the six positions indicated on top, acquired using multi-scan SE, and single-shot SE-EPI, SPEN and xSPEN sequences, respectively. Common scan parameters: FOV = 40 × 40 mm^2; slice thickness = 3 mm; gap = 3 mm; number of slices = 6; matrix size = 64 × 64; acquisition bandwidth = 250 kHz; slice selection pulse gradient = 2.28 G/cm (kept identical for all sequences to preserve the slice selection characteristics). WURST-shaped swept pulses28 were used in (e) and (f); for SPEN their sweep bandwidth = 13.6 kHz and sweep duration = 11.01 ms; for xSPEN sweep bandwidth = 5.8 kHz and sweep duration =11.01 ms. The constant G_z gradient = 2.27 G/cm while the encoding G_y gradient = 0.17 G/cm. As in subsequent figures, the indicated times correspond to the full multi-slice data collection of

Europe PMC Funders Author Manuscripts

each sequence (which for SE-EPI factor in the need for an ancillary navigator scan for each slice).

Europe PMC Funders Author Manuscripts

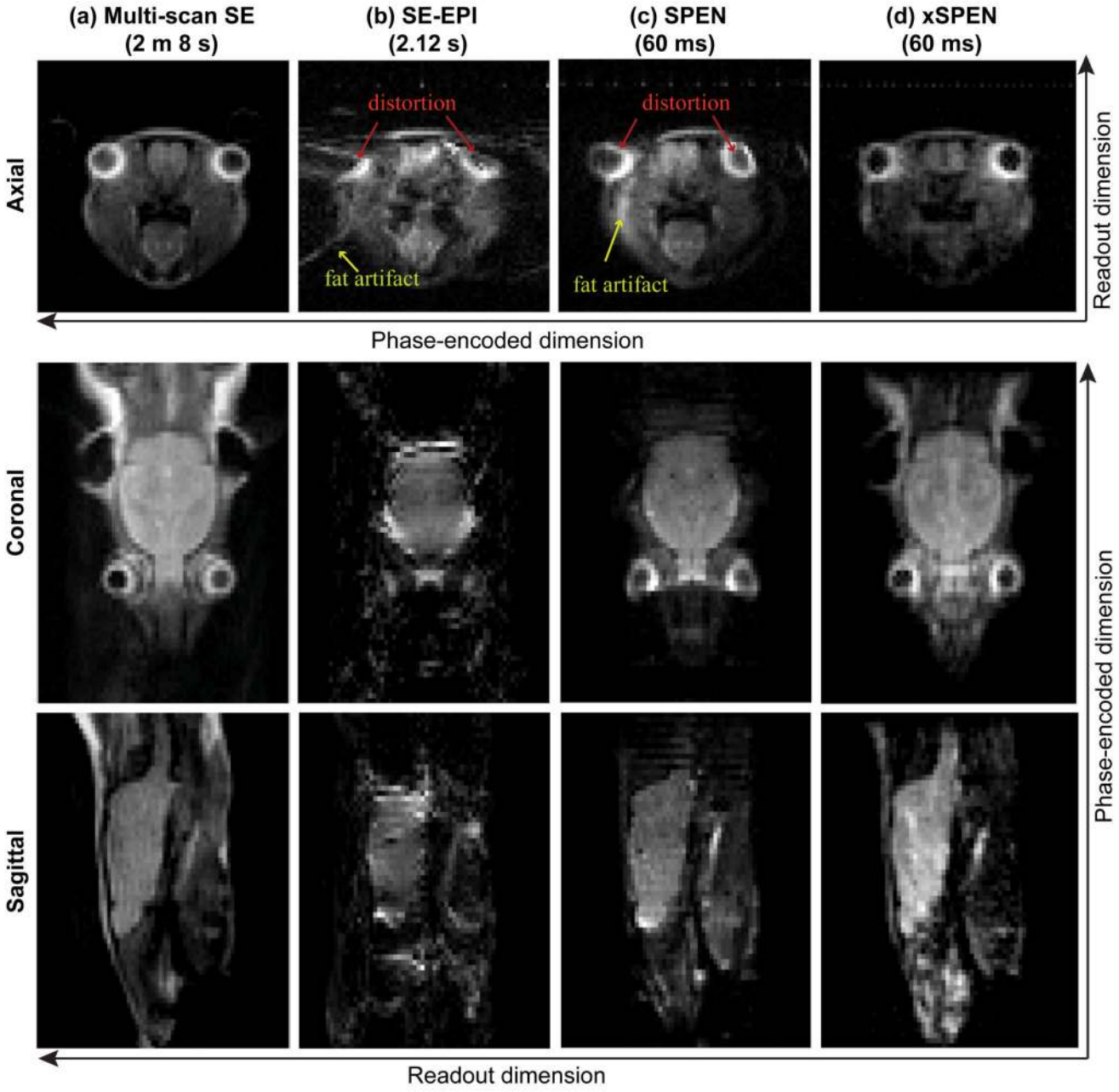

Figure 5.

Three-plane comparisons of *in vivo* head scans acquired on an mouse using (a) a multi-scan SE, (b) SE EPI, (c) SPEN and (d) xSPEN sequences. Average water line widths in these targeted 3D volumes were ca. 80 Hz. Common scan parameters were as follows. For the axial plane: FOV = 25 × 25 mm^2; slice thickness = 4 mm; matrix size = 64 × 64; slice selection pulse gradient = 1.71 G/cm for all sequences. For the coronal and sagittal planes: FOV = 30 × 40 mm^2; slice thickness = 3 mm; matrix size = 64 × 64; slice selection pulse gradient = 2.27 G/cm for all sequences. Acquisition bandwidth = 250 kHz for all experiments. WURST-shaped swept pulses were used for SPEN and xSPEN experiments;

for the former with a bandwidth = 13.6 kHz and duration = 11.01 ms, and for the latter with a sweep bandwidth = 5.8 kHz and sweep duration =11.01 ms. Additional parameters for the xSPEN experiments: constant G_z gradient = 1.71 G/cm and encoding gradient G_y = 0.27 G/cm for the axial plane; G_z = 2.27 G/cm and G_y = 0.17 G/cm for the coronal and sagittal planes.

Europe PMC Funders Author Manuscripts

Europe PMC Funders Author Manuscripts

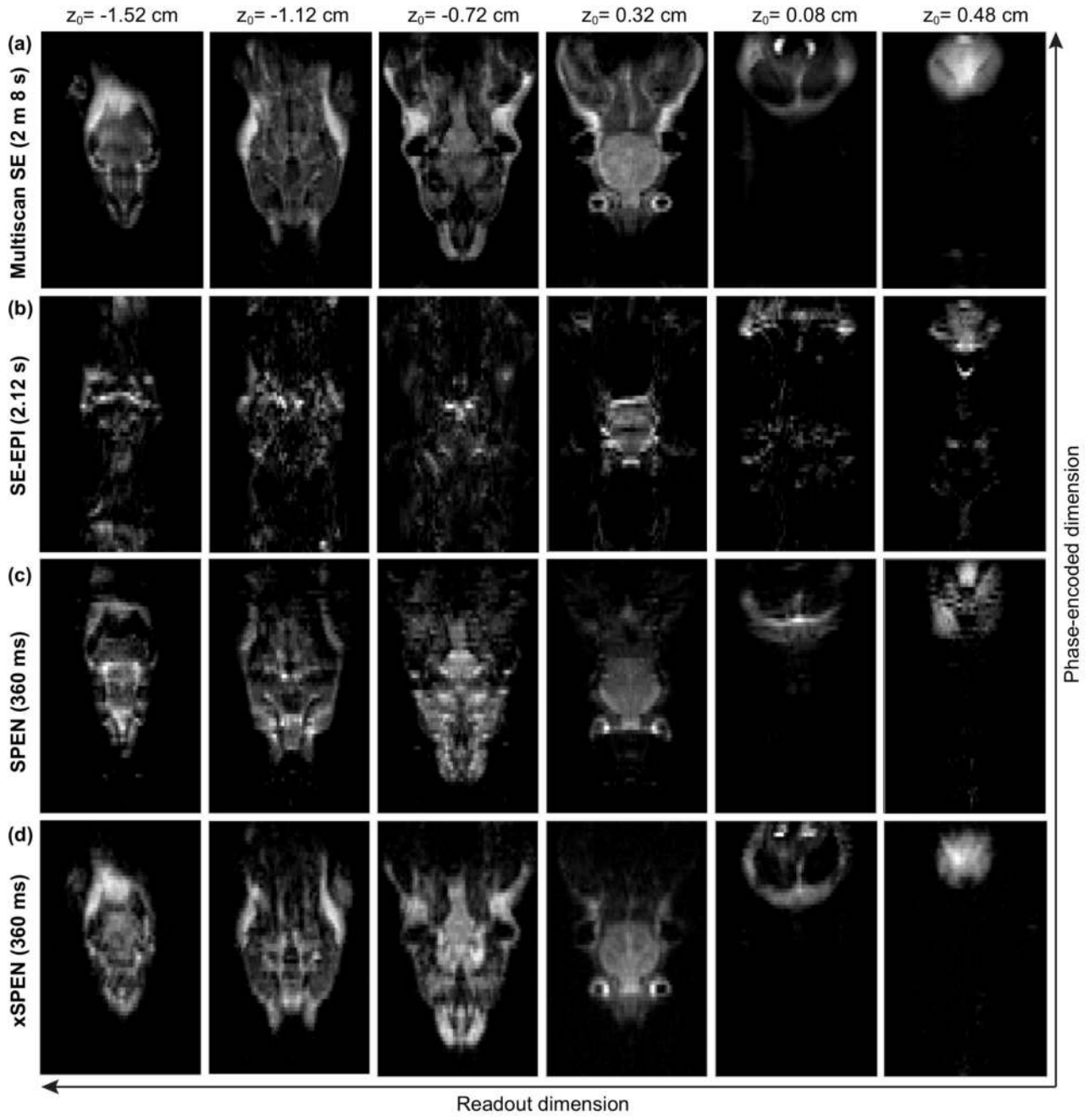

Figure 6.

Comparisons between multi-slice coronal *in vivo* mouse head images collected using (a) a multi-scan SE sequence, (b) SE EPI, (c) SPEN and (d) xSPEN. All experiments were collected using 3 mm thick slices, whose centers were placed 4 mm apart. Common scan parameters: FOV = 30 × 60 mm^2; matrix size = 64 × 64; slice selection gradient = 2.27 G/cm; overall sample volume = ~40 mL. The multi-scan acquisition bandwidth and WURST

pulse parameters were as in Figure 5. For xSPEN a constant G_z gradient = 2.27 G/cm and an encoding G_y gradient = 0.114 G/cm were used.

Europe PMC Funders Author Manuscripts